

# **Spectral Line-by-Line Pulse Shaping of an On-Chip Microresonator Frequency Comb**

**Fahmida Ferdous,<sup>1</sup> Houxun Miao,<sup>2,3\*</sup> Daniel E. Leaird,<sup>1</sup> Kartik Srinivasan,<sup>2</sup> Jian Wang,<sup>1,4</sup>  
Lei Chen,<sup>2</sup> Leo Tom Varghese,<sup>1,4</sup> and Andrew M. Weiner<sup>1,4\*</sup>**

*<sup>1</sup>School of Electrical & Computer Engineering, Purdue University, 465 Northwestern Avenue,  
West Lafayette, Indiana 47907-2035, USA*

*<sup>2</sup>Center for Nanoscale Science and Technology, National Institute of Standards and Technology,  
100 Bureau Dr, Gaithersburg, MD 20899, USA*

*<sup>3</sup>Maryland Nanocenter, University of Maryland, College Park, MD 20742, USA*

*<sup>4</sup>Birck Nanotechnology Center, Purdue University, 1205 West State Street, West Lafayette,  
Indiana 47907, USA*

*\*Corresponding authors: amw@purdue.edu, houxun.miao@nist.gov*

**Recently, on-chip comb generation methods based on nonlinear optical modulation in ultrahigh quality factor monolithic microresonators have been demonstrated, where two pump photons are transformed into sideband photons in a four wave mixing process mediated by the Kerr nonlinearity. Here we investigate line-by-line pulse shaping of such combs generated in silicon nitride ring resonators. We observe two distinct paths to comb formation which exhibit strikingly different time domain behaviors. For combs formed as a cascade of sidebands spaced by a single free**

**spectral range (FSR) that spread from the pump, we are able to stably compress to nearly bandwidth-limited pulses. This indicates high coherence across the spectra and provides new data on the high passive stability of the spectral phase. For combs where the initial sidebands are spaced by multiple FSRs which then fill in to give combs with single FSR spacing, the time domain data reveal partially coherent behavior.**

Optical frequency combs consisting of periodic discrete spectral lines with fixed frequency positions are powerful tools for high precision frequency metrology, spectroscopy, broadband gas sensing, and other applications<sup>1-7</sup>. Frequency combs generated in mode locked lasers can be self-referenced to have both stabilized optical frequencies and repetition rates (with repetition rates below  $\approx 1$  GHz in most cases)<sup>8</sup>. An alternative approach based on strong electro-optic phase modulation of a continuous wave (CW) laser provides higher repetition rates, up to a few tens of GHz, but without stabilization of the optical frequency<sup>9-12</sup>. Recently, a novel method for optical frequency comb generation, known as Kerr comb generation, by nonlinear wave mixing in a microresonator has been reported<sup>13-22</sup>. The essential advantages of Kerr comb generation are simplicity, small size, and very high repetition rate.

Most investigations of Kerr combs have emphasized their spectral properties, including optical and RF frequency stability. A few experiments have reported time domain autocorrelation data<sup>23</sup>. Here we expand the time domain understanding of these devices by manipulating their temporal behavior through programmable optical pulse shaping<sup>24</sup>. The large mode spacing of Kerr combs facilitates pulse shaping at the individual line level, also termed optical arbitrary waveform generation (OAWG)<sup>25-29</sup>, a technology which offers significant opportunities for impact both in technology (e.g., telecommunications, lidar) and ultrafast optical

science (e.g., coherent control and spectroscopy). We demonstrate line-by-line pulse shaping of microresonators based frequency combs. An important feature of our approach is that transform-limited pulses may in principle be realized for any spectral phase signature arising from a coherent comb generation process. Furthermore, the ability to achieve successful pulse compression provides new information on the passive stability of the frequency dependent phase of coherent Kerr combs. Our time-domain experiments also reveal differences in coherence properties associated with different pathways to comb formation.

Fig. 1(a) shows a microscope image of a 40  $\mu\text{m}$  radius silicon nitride microring resonator with coupling waveguide (described in the Methods section). For robust and low-loss coupling of light into and out of the devices, we have developed a process for fiber pigtailed the chip, as shown in Fig. 1(b). The fiber pigtailed used for this device eliminates the time consuming task of free space coupling and significantly enhances transportability. Other devices studied employ a similar V-groove scheme to facilitate coupling alignment, but without permanent fiber attachment.

Spectroscopy of the resonator's optical modes is performed with a swept wavelength tunable diode laser with time-averaged linewidth of less than 5 MHz. Figure 1(c) shows the transmission spectrum of two orders of transverse magnetic (TM) modes (with different free spectral range (FSR) and coupling depth), which have their electric field vectors predominantly normal to the plane of the resonator. Fig. 1(d) shows a zoomed in spectrum for a mode at  $\approx 1556.43$  nm with a line width of 1.2 pm, corresponding to a loaded optical quality factor (Q) of  $1.3 \times 10^6$ . The average FSR of the series of high Q modes is measured to be  $\approx 4.8$  nm. The loaded Qs of the microresonators used in this paper are typically  $1 \times 10^6$  to  $3 \times 10^6$ .

Fig. 2 shows the experimental setup. CW light is launched into the microresonator, with a polarization controller used to align the input polarization with the TM mode. The generated frequency comb is launched to a line-by-line pulse shaper for spectral phase measurement and correction, which are accomplished simultaneously by optimizing the second harmonic generation (SHG) signal<sup>30, 31</sup>, as described in the Methods. The pulse shaper is also used to attenuate the pump line, which in our experiments is typically 10 to 23 dB stronger than the adjacent comb lines, and is sometimes programmed to attenuate some of the neighboring lines as well. This results in a spectrum with line-to-line power variations reduced (but not completely eliminated), which improves time domain pulse quality. In Ref. 31, the phase measurement by this SHG optimization method is compared with another independent method based on spectral shearing interferometry. The difference between the two measurements was comparable to the  $\pi/12$  step size of the SHG optimization method. This provides an estimate of both the precision and the accuracy of our phase measurement method. In addition to autocorrelation measurements which provide information on the temporal intensity, comb spectra are measured both directly after the microresonator and after the pulse shaper and subsequent Erbium doped fiber amplifier (EDFA).

We have investigated comb generation with subsequent line-by-line shaping in a number of devices and have observed two distinct paths to comb formation which exhibit strikingly different time domain behaviors. Comb spectra measured directly after generation are shown in Fig. 3, with estimated optical powers coupled to the access waveguides given in the figure caption. In some cases the comb is observed to form as a cascade of sidebands spaced by approximately one FSR that spread from the pump (Figs. 3(a), 3(b) and 3(c) with comb spacings of  $\approx 600$  GHz, 230 GHz, 115 GHz, respectively). In such cases, which we will refer to as Type I

comb formation, high quality pulse compression is achieved, signifying good coherence properties. In other cases (Figs. 3(d) and 3(f)), the initial sidebands are spaced by multiple FSRs from the pump. With changes in pump power or wavelength, additional lines spread out from each of these initial sidebands, eventually merging to form a spectrum composed of lines separated by approximately one FSR. For example, Fig. 3(d) shows a comb comprising nearly 300 lines spaced by 115 GHz; the initial sidebands, which remain evident as strong peaks, are spaced by approximately 27 FSRs. This route to comb formation, which we will call Type II, has been discussed by several authors<sup>16, 17, 32, 33</sup>. With our devices, Type II formation results in a larger number of lines, but compressibility is degraded in a way that provides clear evidence of partial coherence. Different regimes of comb generation with distinct coherence properties have also recently been reported for combs generated from silica microresonators<sup>34</sup>. In addition, comb linewidth variations with different pumping conditions have also been reported<sup>19</sup>.

Figure 4 shows a first set of pulse shaping results from a 40  $\mu\text{m}$  radius microresonator (Fig. 1(a)) which generates the Type I comb shown in Fig. 3(a), comprising twenty-six comb lines with a repetition rate of  $\approx 600$  GHz. The average output power for an estimated 0.45 W coupled into the input waveguide is measured to be 0.10 W. We select 9 comb lines (limited by the bandwidth of the pulse shaper and the bandwidth of the EDFA before the autocorrelator) to perform the line-by-line pulse shaping experiments. The spectrum after the pulse shaper and the spectral phase profile which is found to maximize the SHG signal are shown in Fig. 4(a). Fig. 4(b) shows the measured autocorrelation traces before and after spectral phase correction. The signal appears nearly unmodulated in time without phase correction, while a clear pulse-like signature is present after correction. Such pulse compression clearly demonstrates successful line-by-line pulse shaping. The intensity profile of the compressed pulse, calculated based on the

spectrum (Fig. 4(a)) assuming a flat spectral phase, has a full width at half maximum (FWHM) of 312 fs. The corresponding intensity autocorrelation trace is calculated (as shown in Fig. 4(b)) and is in good agreement with the experimental trace. The finite signal level remaining between the autocorrelation peaks arises due to the finite number of lines and the uneven profile of the spectrum. The widths of experimental and computed autocorrelation traces are 460 fs and 427 fs, respectively, which differ by 7%. From this we take the uncertainty in our 312 fs pulse duration estimation as  $\pm 7\%$ . As a preliminary example of arbitrary waveform generation, we program the pulse shaper to apply a  $\pi$ -step function to the spectrum of the compressed pulse; Fig. 4(c) shows the result. The  $\pi$  step occurs at the pixel number 64 (corresponds to 1550 nm in wavelength). Application of a  $\pi$  phase step onto half of the spectrum is known to split an original pulse into an electric field waveform that is antisymmetric in time, sometimes termed an odd pulse<sup>35</sup>. The resulting autocorrelation triplet is clearly visible as shown in Fig. 4(c) and in good agreement with the autocorrelation that is computed based on the spectrum in Fig. 4(a) and a spectral phase that is flat except for a  $\pi$ -step centered at 1550 nm. This result constitutes a clear example of line-by-line pulse shaping for simultaneous compression and waveform shaping.

Similar high quality pulse compression results have been achieved with other devices exhibiting Type I comb formation. Figure 5 shows data for larger silicon nitride ring resonators (200  $\mu\text{m}$  and 100  $\mu\text{m}$  radii) which generate combs spaced by 115 GHz (Fig. 3(c)) and 230 GHz (Fig. 3(b)), respectively. These devices have fiber to fiber coupling loss as low as 3 dB when lensed fibers are used. The comb spectrum obtained for pumping the 200  $\mu\text{m}$  radius device at  $\approx 1547$  nm exhibits 12 spectral lines, covering  $\approx 10$  nm bandwidth. The comb spectrum obtained for pumping the 100  $\mu\text{m}$  radius device at  $\approx 1549$  nm exhibits 25 spectral lines, covering  $\approx 45$  nm

bandwidth (20 spectral lines are left after the shaper). The autocorrelation data again show that although originally the signals are at most weakly modulated in time, phase correction results in obvious compression into pulse-like waveforms, yielding autocorrelation FWHMs of 1.78 ps and 976 fs for 200  $\mu\text{m}$  and 100  $\mu\text{m}$  rings, respectively. In both cases the shape and on-off contrasts of the autocorrelation are in fairly close agreement with the results simulated using the measured spectra and assuming flat spectral phase.

Time domain experiments access information about coherence that is not available from frequency domain data such as the comb spectra. For example, the ability to achieve pulse compression and phase shaping results as shown in Figs. 4 and 5 provides clear evidence of coherence across the comb spectrum. Note that intensity autocorrelation measurements are insensitive both to overall optical phase and to optical phase that varies linearly with frequency. Small changes in pulse repetition rate that would arise from small changes in comb spacing would also be difficult to observe from autocorrelation data (provided that the comb spacing remains uniform across the spectrum). However, autocorrelations do provide information on changes in pulse duration associated with spectral phase variations quadratic or higher in frequency. The close agreement in the shape and on-off contrast of experimental autocorrelation traces, compared with those calculated on the basis of the measured comb spectra (with flat spectral phase), provides evidence that the obtained pulses are not only close to bandwidth-limited, but also that they have high coherence. We also observe the autocorrelations over an extended period. Fig. 4(d) shows autocorrelation traces measured at different times within a 62 minute interval, with the same spectral phase profile applied by the pulse shaper for all measurements. Clearly the compression results remain similar over the one hour time period indicated in the figure, which means that the relative average phases of the comb lines must

remain approximately fixed; slow drifts in relative average spectral phase must conservatively remain substantially below  $\pi$ . Assume now that the field consists of lines at frequencies  $f_o + n f_{rep} + \delta f_n$ , where  $f_o$  is the carrier-envelope offset frequency,  $f_{rep}$  is the repetition rate and the  $\delta f_n$  refer to small fixed shifts (assumed to be random and uncorrelated) of the individual frequencies from their ideal, evenly spaced positions. Such frequency shifts would give rise to phase errors for the different spectral lines that grow in time according to  $\delta \varphi_n = 2\pi \delta f_n t$ . Since the  $\delta f_n$ , and hence the linear drifts of the  $\delta \varphi_n$ , are taken as uncorrelated, the characteristic size of the phase errors should (conservatively) satisfy  $|\delta \varphi_n| < 0.7\pi$  in order to avoid significant waveform changes. With 3600 s observation time, we may then estimate that the assumed  $\delta f_n$  are conservatively of the order  $10^{-4}$  Hz or below. Our estimation is consistent with measurements performed for combs from silica microtoroids, by beating with a self-referenced comb from a mode-locked laser, which indicated uniformity in the comb spacing at least at the  $10^{-3}$  Hz level<sup>14</sup>.

In contrast to the data presented so far for Type I combs, for which the time domain data indicate good coherence, we now discuss our observations for Type II combs, in which the initial sidebands are spaced by multiple FSRs from the pump. First we discuss the compression experiments for a Type II comb obtained from a 200  $\mu\text{m}$  radius ring pumped at  $\approx 1549$  nm, with the directly generated spectrum of Fig. 3(d). We performed pulse compression experiments on a group of 24 comb lines centered at  $\approx 1558$  nm. The spectrum after smoothing and phase correction is shown in Fig. 6(a), and the autocorrelation data are shown in Fig. 6(d). Once again phase compensation results in substantial compression compared to the original waveform which shows only weak modulation. However, a new feature is that the on-off contrast of the experimental autocorrelation is significantly worse than the simulated trace which assumes phases that are frequency independent and constant in time. The significantly degraded

autocorrelation contrast is a hallmark of partial coherence, which can occur when the spectral phase function varies in a nontrivial way during the measurement time.

It is known that the autocorrelation of continuous intensity noise consists of a single peak centered at zero delay on top of a constant positive background<sup>36,37</sup>. For a Gaussian random field with phases completely randomized, the ratio of the peak value to the background is 2:1. The width of the autocorrelation peak gives the time scale for the intensity fluctuations and does not imply the existence of a meaningful pulse duration. Furthermore, the shape of the autocorrelation will not be affected by spectral phase shaping. On the other hand, a coherent train of periodic pulses shows a series of peaks at delays corresponding to the pulse separation and exhibits high autocorrelation contrast. The autocorrelation trace does provide information on the pulse duration and may definitely be changed by spectral phase shaping. In our experiments with Type II combs, the autocorrelation shows contrast better than 2:1, but significantly less than would be expected with perfect phase compensation. The portion of the autocorrelation above the background remains responsive to spectral phase shaping and allows compression to bandwidth-limited peaks which repeat at the inverse of the comb spacing. This behavior corresponds to fluctuations of the spectral phase on a time scale fast compared to the measurement time and with amplitude that is significant but less than  $2\pi$ , or in other words, partial coherence. In this regime the signal consists of a deterministic average waveform superimposed with fluctuating noise-like waveforms with the same repetition period. As explained in the Supplementary Information, a rough estimate of the amplitude of the spectral phase fluctuations may be obtained from the autocorrelation contrast. From the data in Fig. S1, we estimate uncorrelated variations of the spectral phase over an approximate range of  $\pm 0.4\pi$ .

We have observed similar autocorrelation data characteristic of partial coherence in a number of experiments with Type II combs, with minima of the experimental autocorrelation traces lying above the simulated ones assuming full coherence by 17-28% relative to the peak. The uncertainty in simulated traces is estimated by repeating the simulations for 10-20 spectra recorded sequentially during the autocorrelation measurement. The simulated traces with largest positive and negative variation in contrast are shown as light gray lines in Fig. 6(d); this variation is significantly less than that observed experimentally. In contrast, experimental autocorrelations for Type I combs exhibit minima at most 5% above simulated traces. This difference is sufficiently small that it may arise from a combination of effects such as uncertainty or variation in power spectra used for simulations, imperfect compensation of average spectral phase, and in some cases contributions from amplified spontaneous emission (ASE). Although we cannot rule out some level of fast phase fluctuations, our Type I combs clearly exhibit significantly lower phase fluctuations and higher coherence than Type II combs.

Fig. 6(e)-(f) shows another interesting example obtained with 100  $\mu\text{m}$  radius rings (for directly generated spectra, see Figs. 3(e)-(f)). Here we pump a mode at  $\approx 1551.67$  nm, which most readily generates stable comb spectra at 460 GHz spacing (twice the FSR). The spectrum after shaping and amplification comprises eight lines as shown in Fig. 6(b), and the experimental and simulated autocorrelation traces exhibit comparable contrast in Fig. 6(e). Thus, the coherence of this comb appears to be high, similar to Type I combs. However, if the pump wavelength is tuned sufficiently while maintaining lock<sup>38</sup> to the same resonance, the spectrum broadens and intermediate comb lines fill in, resulting in a Type II comb with 230 GHz spacing. Directly generated and post-shaper spectra and the autocorrelation traces are shown in Figs. 3(f), 6(c) and 6(f) for pumping at  $\approx 1551.74$  nm, a large shift compared to the low power linewidth.

Although the shapes of the compressed and simulated autocorrelation traces are similar, with a FWHM of 432 fs, the experimental background level is significantly increased, again indicating reduced coherence for Type II combs. This example demonstrates important coherence differences in combs generated from the same resonance in the same device under different pumping conditions.

In summary, we have demonstrated line-by-line pulse shaping on frequency combs generated from silicon nitride microring resonators. Combs formed via distinct routes (Types I and II in the text) represent different time domain behaviors corresponding to coherent and partially coherent properties. For Type I combs, nearly bandwidth-limited optical pulses were achieved after spectral phase correction, and a simple example of arbitrary waveform generation was presented. For type II combs, compressed pulse trains were accompanied by significant autocorrelation background, signifying larger spectral phase fluctuations. The ability to controllably compress and reshape combs generated through nonlinear wave mixing in microresonators provides new evidence of phase coherence (or partial coherence) across the spectrum. Furthermore, in future investigations the ability to extract the phase of individual lines may furnish clues into the physics of the comb generation process.

## **Methods:**

**Device fabrication:** We started with a (100) silicon wafer. A 3  $\mu\text{m}$  thick silicon dioxide layer was grown in a thermal oxidation furnace. Then, a silicon nitride layer was deposited using low-pressure chemical vapour deposition (LPCVD). The nitride layer was patterned with electron-beam lithography and etched through using a reactive ion etch (RIE) of  $\text{CHF}_3/\text{O}_2$  to form microring resonators and waveguides coupling light into

and out of the resonators. The waveguides were linearly tapered down to a width of  $\approx 100$  nm at their end for low loss coupling to/from optical fibers<sup>39</sup>. Another 3  $\mu\text{m}$  oxide layer was deposited using a low temperature oxide (LTO) furnace for the top cladding. The wafer was annealed for 3 h at 1200  $^{\circ}\text{C}$  in an ambient  $\text{N}_2$  environment. A photolithography and liftoff process was used to define a metal mask for V-grooves that provide self-aligned regions where the on-chip waveguide inverse tapers are accessible by optical fibers placed in the V-grooves. After mask definition, the V-grooves were formed by RIE of the unprotected oxide and nitride layers and KOH etching of the silicon. The height of the ring resonators is 430 nm and 550 nm for devices corresponding to Figure 3(a), and Figure 3(b) to 3(f), respectively. The widths of the rings and of the accessing waveguides are 2  $\mu\text{m}$  and 1  $\mu\text{m}$  throughout the paper. The radii indicated within the paper are those at the outermost edge of the devices. The gap between the ring and the waveguide is 700 nm in Fig 3(a), 500 nm in Fig 3(b), and 800 nm in Fig 3(c)-(f); the difference in ring-waveguide gap will modify the device coupling.

**Experimental procedure:** Microresonators are pumped with CW powers estimated between 66 mW to 1.4 W coupled into the input guide, in all cases well above the threshold for comb formation. Line-by-line pulse shaping is implemented using a fiber-coupled Fourier-transform pulse shaper that incorporates a  $2 \times 128$  pixel liquid crystal modulator (LCM) array to independently control both the intensity and phase of each spectral line. The output waveform from the pulse shaper is fed to an intensity autocorrelation setup through an EDFA. The path from the output of the microring chip to the autocorrelator comprises  $\approx 18$  m of standard single mode fiber (SMF). The

thickness of the BBO crystal used for SHG is 0.6 mm, corresponding to an estimated 1-dB phase matching bandwidth of 200 nm, well beyond the bandwidth of the combs investigated here. Briefly, the phase is corrected by adjusting the phase of one comb line at a time to maximize the SHG signal from the autocorrelation measurement at zero delay. To optimize the SHG signal, the phase of the new frequency component is varied from 0 to  $2\pi$  in steps of  $\pi/12$ . Once the SHG is optimized, the pulses are compressed close to the bandwidth limit, and the opposite of the phase applied on the pulse shaper gives an estimate of the original spectral phase after the comb has propagated to the autocorrelator.

## References

1. Udem, T., Holzwarth, R. and Hänsch, T.W. Optical frequency metrology. *Nature* **416**, 233-237 (2002).
2. Diddams, S.A., Bergquist, J.C., Jefferts, S.R. and Oates, C.W. Standards of Time and Frequency at the Outset of the 21st Century. *Science* **306** (5700), 1318-1324 (2004).
3. Keilmann, F., Gohle, C. and Holzwarth, R. Time-domain mid-infrared frequency-comb spectrometer. *Opt. Lett.* **29**, 1542-1544 (2004).
4. Schliesser, A., Brehm, M., Keilmann, F. and Weide, D.W. van der. Frequency-comb infrared spectrometer for rapid, remote chemical sensing. *Opt. Express*, **13**, 9029-9038 (2005).
5. Diddams, S.A., Hollberg, L. and Mbele, V. Molecular fingerprinting with the resolved modes of a femtosecond laser frequency comb. *Nature* **445**, 627-630 (2007).
6. Thorpe, M.J., Moll, K.D., Jones, J.J., Safdi, B. and Ye, J. Broadband cavity ringdown spectroscopy for sensitive and rapid molecular detection. *Science* **311**, 1595-1599 (2006).
7. Coddington, I., Swann, W.C. and Newbury, N.R. Coherent Multiheterodyne Spectroscopy Using Stabilized Optical Frequency Combs. *Phy. Rev. Lett.* **100**, 013902 (2008).
8. Jones, D. J. *et al.* Carrier-envelope phase control of femtosecond mode-locked lasers and direct optical frequency synthesis. *Science* **288** (5466), 635-639 (2000).
9. Murata, H., Morimoto, A., Kobayashi, T. and Yamamoto, S. Optical pulse generation by electrooptic-modulation method and its application to integrated ultrashort pulse generators. *IEEE J. Sel. Top. Quantum Electron.* **6**, 1325-1331 (2000).

10. Yamamoto, T., Komukai, T., Suzuki, K. and Takada, A. Spectrally flattened phase-locked multi-carrier light generator with phase modulators and chirped fibre Bragg grating. *Electron. Lett.* **43**, 1040-1042 (2007).
11. Wu, R., Supradeepa, V.R., Long, C.M., Leaird, D.E. and Weiner, A.M. Generation of very flat optical frequency combs from continuous-wave lasers using cascaded intensity and phase modulators driven by tailored radio frequency waveforms. *Opt. Lett.* **35**, 3234-3226 (2010).
12. Kourogi, M., Nakagawa, K. and Ohtsu, M. Wide-span optical frequency comb generator for accurate optical frequency difference measurement. *IEEE J. Quantum Electron.* **29**, 2693-2701 (1993).
13. Kippenberg, T.J., Holzwarth, R. and Diddams, S.A. Microresonator-based optical frequency combs, *Science*, **332**, 555-559 (2011).
14. DelHaye, P. *et al.* Optical frequency comb generation from a monolithic microresonator. *Nature* **450**, 1214-1217 (2007).
15. Levy, J.S. *et al.* Cmos-compatible multiple-wavelength oscillator for on-chip optical interconnects. *Nature Photon.* **4**, 37-40 (2010).
16. Razzari, L. *et al.* Cmos compatible integrated optical hyper-parametric oscillator. *Nature Photon.* **4**, 41-45 (2010).
17. Grudinin, I.S., Yu, N. and Maleki, L. Generation of optical frequency combs with a CaF<sub>2</sub> resonator. *Opt. Lett.* **34**, 878-880 (2009).
18. P. DelHaye, O. Arcizet, A. Schliesser, R. Holzwarth, and T.J. Kippenberg, Full stabilization of a microresonator-based optical frequency comb. *Phy. Rev. Lett.* **101**, 053903 (2008).

19. P. Del'Haye, T. Herr, E. Gavartin, M. L. Gorodetsky, R. Holzwarth, and T.J. Kippenberg, Octave spanning tunable frequency comb from a microresonator. *Phy. Rev. Lett.* **107**, 063901 (2011).
20. Foster, M.A. *et al.* Silicon-based monolithic optical frequency comb source. *Opt. Express*, **19**, 14233-14239 (2011).
21. Okawachi, Y. *et al.* Octave-spanning frequency comb generation in a silicon nitride chip, arXiv: 1107.5555 (2011).
22. Ferrera, M. *et al.* Low power four wave mixing in an integrated, micro-ring resonator with  $Q = 1.2$  million. *Optics Express*, **17**, 14098-14103 (2009).
23. Arcizet, O., Schliesser, A., Del'Haye, P., Holzwarth, R., and Kippenberg, T. J., Optical Frequency Comb Generation in Monolithic Microresonators. in *Practical Applications of Microresonators in Optics and Photonics*. (Taylor & Francis Group, LLC, 2009).
24. Weiner, A.M. Femtosecond pulse shaping using spatial light modulators. *Rev. Sci. Instrum.* **71**, 1929-1960 (2000).
25. Jiang, Z., Seo, D.S., Leaird, D.E. and Weiner, A.M. Spectral line by line pulse shaping. *Opt. Lett.* **30**, 1557-1559 (2005).
26. Miyamoto, D. *et al.* Waveform-controllable optical pulse generation using an optical pulse synthesizer. *IEEE Photon. Technol. Lett.* **18**, 721-723 (2006).
27. Jiang, Z., Huang, C.-B., Leaird, D.E. and Weiner, A.M. Optical arbitrary waveform processing of more than 100 spectral comb lines. *Nature Photon.* **1**, 463-467 (2007).
28. Fontaine, N.K. *et al.* 32 phase $\times$ 32 amplitude optical arbitrary waveform generation. *Opt. Lett.* **32**, 865-867 (2007).
29. Cundiff, S.T. and Weiner, A.M. Optical arbitrary waveform generation. *Nature Photon.* **4**, 760-766(2010).

30. Huang, C.B., Park, S.G., Leaird, D.E. and Weiner, A.M. Nonlinearly broadened phase-modulated continuous-wave laser frequency combs characterized using DPSK decoding. *Opt. Express* **16**, 2520-2527(2008).
31. Miao, H., Leaird, D.E., Langrock, C., Fejer, M.M. and Weiner, A.M. Optical Arbitrary Waveform Characterization via Dual-quadrature Spectral Shearing Interferometry. *Opt. Express* **17**, 3381-3389 (2009).
32. Chembo, Y. K., Strekalov, D. V. and Yu N. Spectrum and Dynamics of Optical Frequency Combs Generated with Monolithic Whispering Gallery Mode Resonators. *Phy. Rev. Lett.* **104**, 103902 (2010).
33. Agha, I.H., Okawachi, Y. and Gaeta, A.L., Theoretical and experimental investigation of broadband cascaded four-wave mixing in high-Q microspheres. *Opt. Express* **17**, 16209-16215 (2009).
34. Papp, S. B. and Diddams, S. A. Spectral and temporal characterization of a fused-quartz microresonator optical frequency comb. arXiv: 1106.2487v1 (2011).
35. Heritage, J.P., Weiner, A.M. and Thurston, R.N. Picosecond Pulse Shaping by Spectral Phase and Amplitude Manipulation. *Opt. Lett.* **10**, 609-611 (1985).
36. Ippen, E. P. and Shank, C. V. *Ultrashort Light Pulses*. (Springer-Verlag, New York, 1977).
37. Weiner, A. M. *Ultrafast Optics*. (John Wiley & Sons, Inc., 2009).
38. Carmon, T., Yang, L. and Vahala, K.J. Dynamic thermal behavior and thermal self-stability of microcavities. *Opt. Express*, 12, 4742-4750 (2004).
39. Shoji, T., Tsuchizawa, T., Watanabe, T., Yamada, K. and Morita, H. Low loss mode size converter from 0.3  $\mu\text{m}$  square Si wire waveguides to single mode fibres. *Electron. Lett.* **38**, 1669-1670 (2002).

## **Acknowledgements:**

We gratefully acknowledge Vladimir Aksyuk, Minghao Qi, Chris Long and Victor Torres Company for their comments and suggestions and thank the staff of the CNST Nanofab, especially Richard Kasica, for assistance with E-beam lithography. This project was supported in part by the National Science Foundation under grants ECCS-0925759 and ECCS-1102110 and by the Naval Postgraduate School under grant N00244-09-1-0068 under the National Security Science and Engineering Faculty Fellowship program. Any opinion, findings, and conclusions or recommendations expressed in this publication are those of the authors and do not necessarily reflect the views of the sponsors.

## **Author Contributions**

FF led pulse shaping and compression experiments with the assistance of DEL, HM, and JW. HM led device fabrication with the assistance of LC. FF, KS, and LTV participated in microring design and/or characterization. AMW and HM organized and coordinated the project. AMW, HM, FF, DEL, and KS contributed to the writing.

**Figure 1 High Q silicon nitride microring.** (a) Microscope image of a 40  $\mu\text{m}$  radius microring with the coupling region. (b) Image of a fiber pigtail. (c) Transmission spectrum of the microring resonator. (d) Zoomed in spectrum of an optical mode with a 1.2 pm linewidth.

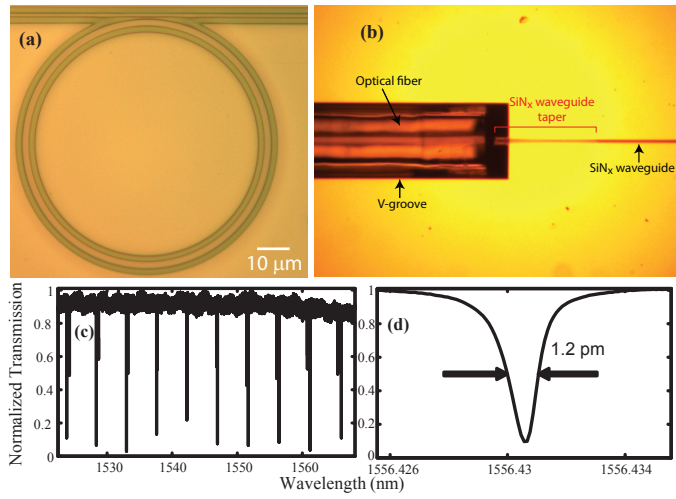
**Figure 2 Experimental Setup.** Scheme of the experimental setup for line-by-line pulse shaping of a frequency comb from a silicon nitride microring. CW: continuous-wave; EDFA: erbium doped fiber amplifier; FPC: fiber polarization controller;  $\mu\text{ring}$ : silicon nitride microring; OSA: optical spectrum analyzer.

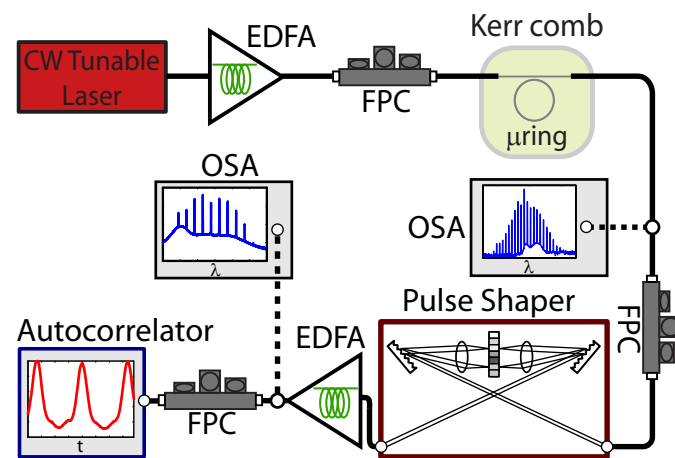
**Figure 3 Generated Kerr frequency comb from silicon nitride rings.** Spectra of generated optical frequency combs. For each spectrum the CW pump wavelength, estimated power coupled to the access waveguide, and ring radius will be succinctly indicated (a) 1543.07 nm, 0.45 W, 40  $\mu\text{m}$ ; (b) 1548.63 nm, 66 mW, 100  $\mu\text{m}$ ; (c) 1547.15 nm, 1.4 W, 200  $\mu\text{m}$ ; (d) 1549.26 nm, 1.4 W, 200  $\mu\text{m}$ ; (e) 1551.67 nm, 1.4 W, 100  $\mu\text{m}$ ; and (f) 1551.74 nm, 1.4 W, 100  $\mu\text{m}$ .

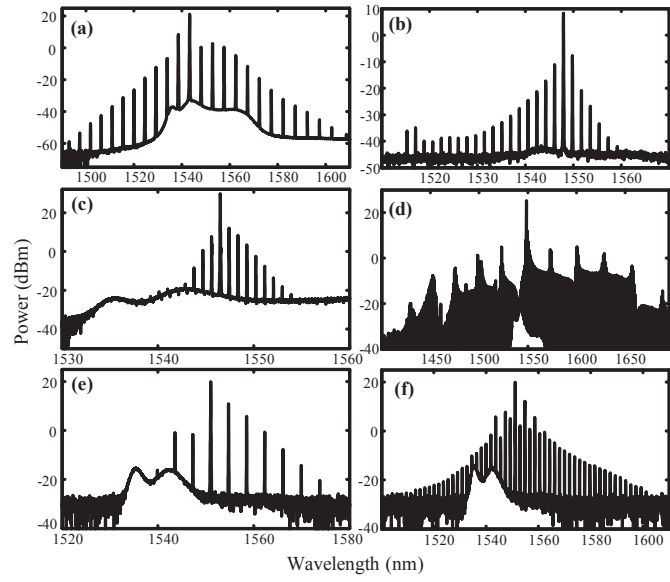
**Figure 4 Optical arbitrary waveform generation from a Kerr comb.** (a) Spectrum of the generated comb (Fig. 3(a)) after the pulse shaper, along with the phase applied to the LCM pixels of the pulse shaper for optimum SHG. (b) Autocorrelation traces. Here the red line is the compressed pulse, the dark blue line is the uncompressed pulse, and the black line is calculated by taking the spectrum shown in Fig. 4(a) and assuming flat spectral phase. The contrast ratio of the autocorrelation measured after phase compensation is 7:1. (c) The odd pulse: applied the same phase as Fig. 4(a), but with an additional  $\pi$  phase added for pixels 1-64 (wavelengths longer than 1550 nm). Red line: experimental autocorrelation; black line: autocorrelation calculated using the spectrum of Fig. 4(a), with a  $\pi$  step centered at 1550 nm in the spectral phase. (d) Normalized intensity autocorrelation traces for compressed pulses, measured at 0, 14, and 62 minutes after spectral phase characterization, respectively.

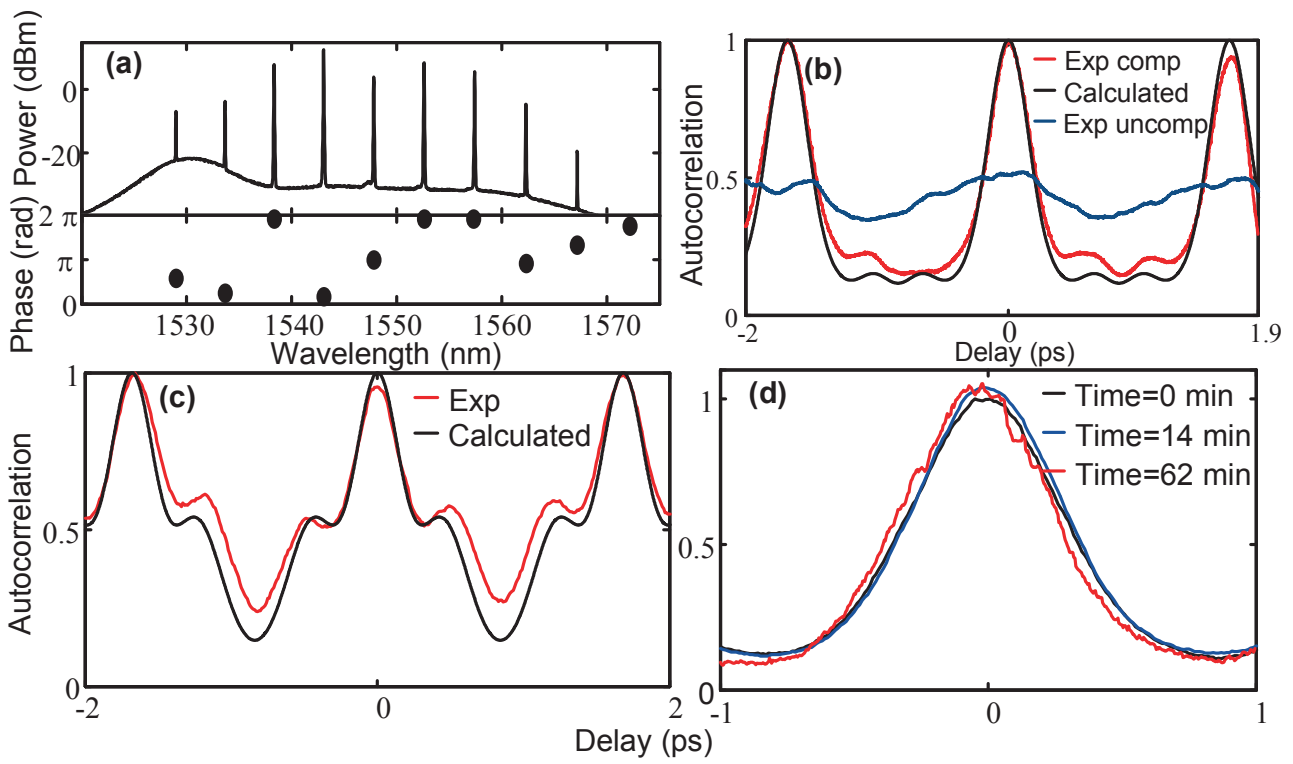
**Figure 5 Compressed pulses of type I Kerr combs.** (a) and (b) Spectra of the generated combs (corresponding to Fig. 3(c) and 3(b), respectively) after the pulse shaper, along with the phase applied to the LCM pixels for optimum SHG signals. (c) and (d) Autocorrelation traces corresponding to (a) and (b). Red lines are the compressed pulses after phase correction, dark blue lines are the uncompressed pulses, and black lines are calculated by taking the spectra shown in (a) and (b) and assuming flat spectral phase. The contrast ratios of the autocorrelations measured after phase compensation are 14:1 and 12:1, respectively. Here Light gray traces show the range of simulated autocorrelation traces.

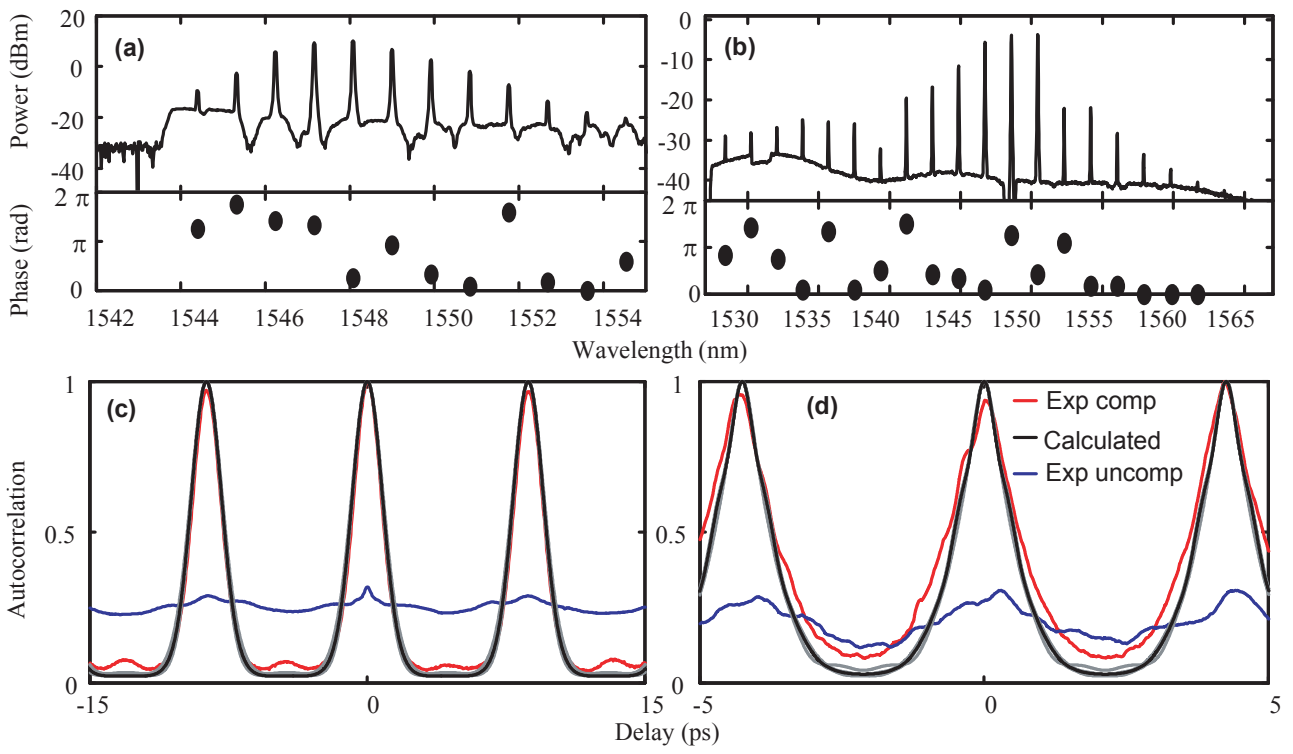
**Figure 6 Compressed pulses of type II Kerr combs.** (a), (b) and (c) Spectra of the generated comb (corresponding to Fig. 3(d), 3(e) and 3(f), respectively) after the pulse shaper, along with phase applied to the LCM pixels for optimum SHG signals. (d), (e) and (f) Autocorrelation traces corresponding to (a), (b) and (c). Red lines are the compressed pulse after phase correction, dark blue lines are the uncompressed pulse, and black lines are the calculated trace by taking the spectrum shown in (a), (b) and (c) and assuming flat spectral phase. Here Light gray traces show the range of simulated autocorrelation traces.

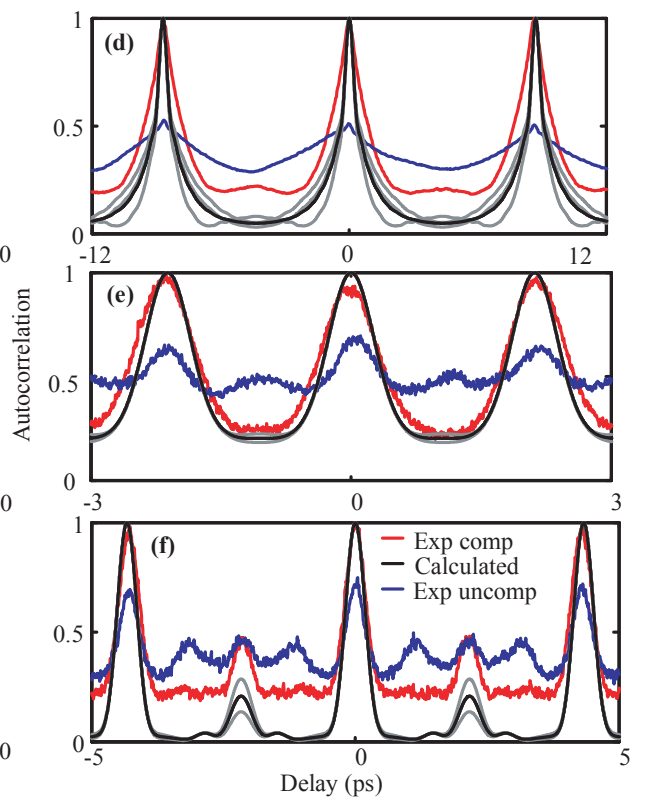
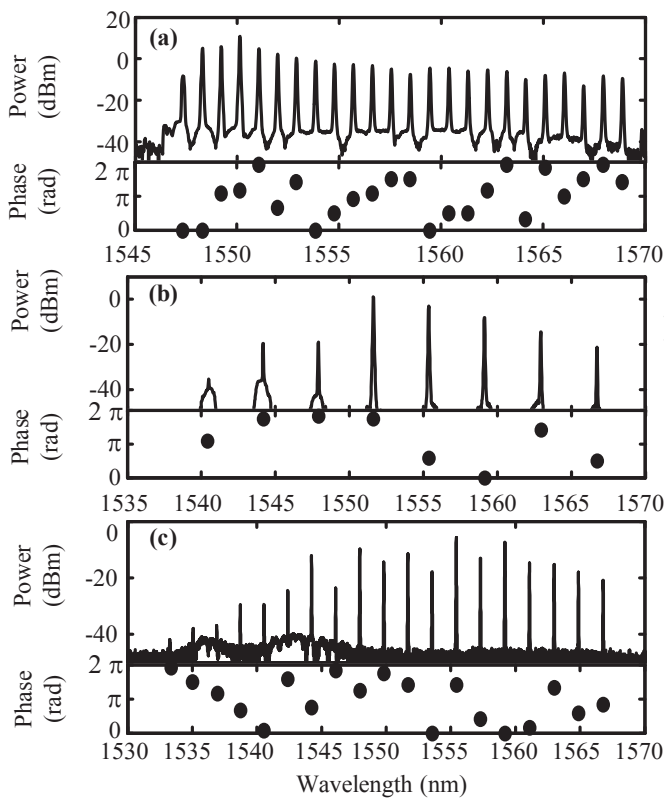












## Supplementary Information

Here, we briefly discuss the effect of variations of the phase of each of the comb lines on the intensity autocorrelation. Simulations are performed by taking the spectrum measured with an optical spectrum analyzer (OSA), assuming that the spectral phase is flat, and then applying an uncorrelated random phase variation to each of the comb lines. The intensity autocorrelation is then calculated. This is repeated for different realizations of the phase variations, while keeping the same phase variation statistics. Then the results are averaged to obtain the autocorrelation trace in the presence of time varying spectral phases that are averaged in the experimental measurement procedure.

The temporal intensity  $I_i(t)$  for the  $i^{th}$  realization is given by:

$$I_i(t) = \left| \sum_n \sqrt{p_n} e^{\phi_{ni}} e^{jn\Delta\omega t} \right|^2,$$

where  $p_n$  is the power of the  $n^{th}$  comb line, as obtained from the spectrum,  $\Delta\omega$  is the comb spacing in angular frequency unit, and  $\phi_{ni}$  represents the random phase applied to the  $n^{th}$  comb line in the  $i^{th}$  realization. The  $\phi_{ni}$  are uniformly distributed in the range of 0 to  $\Delta\phi$  and are mutually uncorrelated. The intensity autocorrelation for the  $i^{th}$  realization,  $G_{2i}$ , is given by:

$$G_{2i}(\tau) = \int I_i(t) I_i(t - \tau) dt.$$

The  $G_{2i}$  are not normalized since different realizations of intensity waveforms with different peak to average power ratios will contribute differently to the autocorrelation signals. The simulated autocorrelation is obtained by averaging  $N$  realizations as,

$$G_2(\tau) = \frac{\sum_{i=1}^N G_{2i}(\tau)}{\sum_{i=1}^N G_{2i}(0)} .$$

We show simulations based on the comb spectrum shown in Fig. 6(c). The  $\phi_{ni}$  are assumed to be uniformly distributed between 0 and a maximum phase variation  $\Delta\phi$ . Simulations are performed for  $\Delta\phi = 0, 0.2\pi, 0.4\pi, 0.6\pi, 0.8\pi$ , and  $\pi$ . For each value of  $\Delta\phi$ , we average  $N=2000$  realizations of the unnormalized autocorrelations. Fig. S1 shows the averaged autocorrelation traces. The backgrounds of the autocorrelation traces clearly increase with increased  $\Delta\phi$ . However, the shape of the autocorrelation is not very sensitive to  $\Delta\phi$ . The background level for  $\Delta\phi = 0.8\pi$  matches that of the experimental autocorrelation trace of Fig. 6(f). Although this gives a rough estimate of the amplitude of the phase fluctuations for the experiments of Figs. 6(c) and 6(f), we note that this estimate is not necessarily precise since the form of the phase fluctuation statistics is not known. For these simulations we postulated phase fluctuations that are uniformly distributed, uncorrelated, and with the same statistics for all the lines, but there is no reason to believe this particular assumption holds in the experiments.

To provide some further insights, in Fig. S2, we show four examples of the intensity profiles  $I_i(t)$  obtained with  $\Delta\phi = 0.8\pi$ . These traces are normalized to the peak intensity of the zero phase fluctuation trace. The four intensity profiles are selected for: (a) peak intensity below average, (b) highest peak intensity, (c) lowest peak intensity, and (d) approximately average peak intensity, relative to the 2000 realizations for  $\Delta\phi = 0.8\pi$ . Although the intensity remains periodic in time and in all cases some peak to average power ratios are maintained, we clearly see that the instantaneous intensity waveform is strongly affected by uncorrelated phase fluctuations. Since the integrated intensity remains constant, those intensity realizations with

lower peak intensity are accompanied by higher energy between peaks, which contributes to the increased background level of the autocorrelation traces.

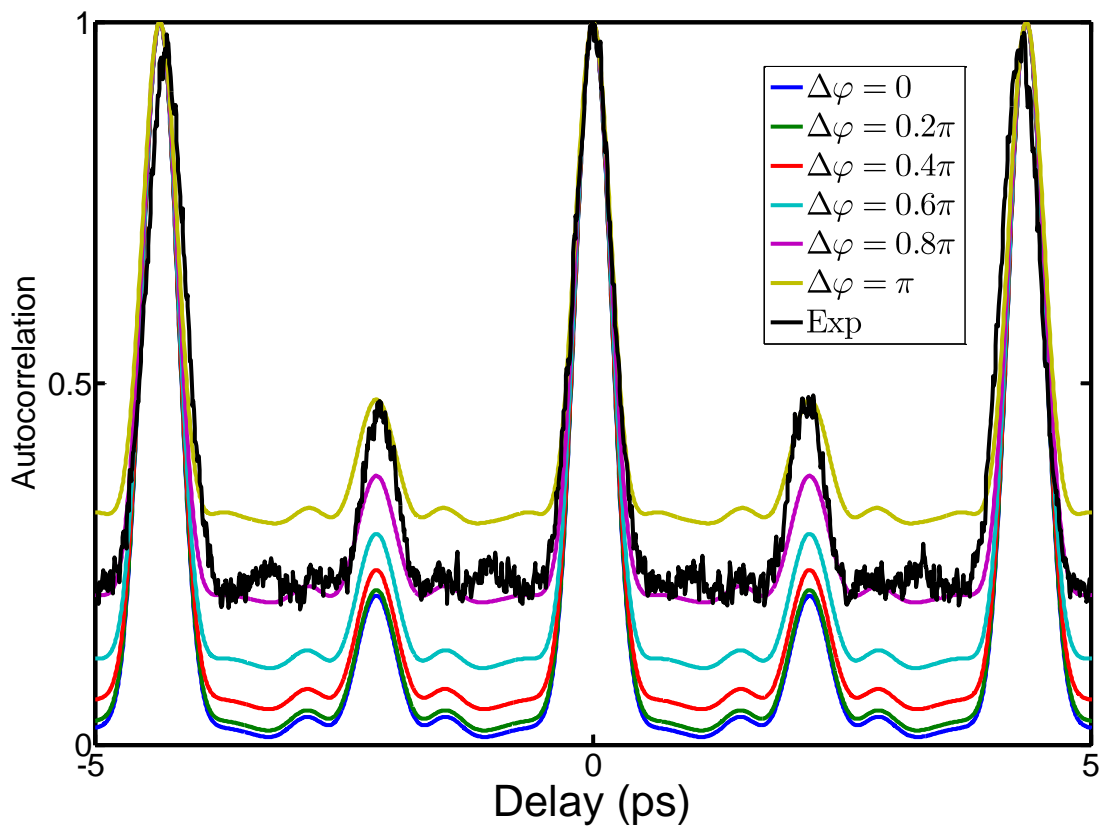


Fig. S1 Simulated intensity autocorrelation traces in which uncorrelated random spectral phases are uniformly distributed in the range of 0 to  $\Delta\varphi$ , for various values of  $\Delta\varphi$ . The experimental autocorrelation trace from Fig. 6(f) is also plotted (black line).

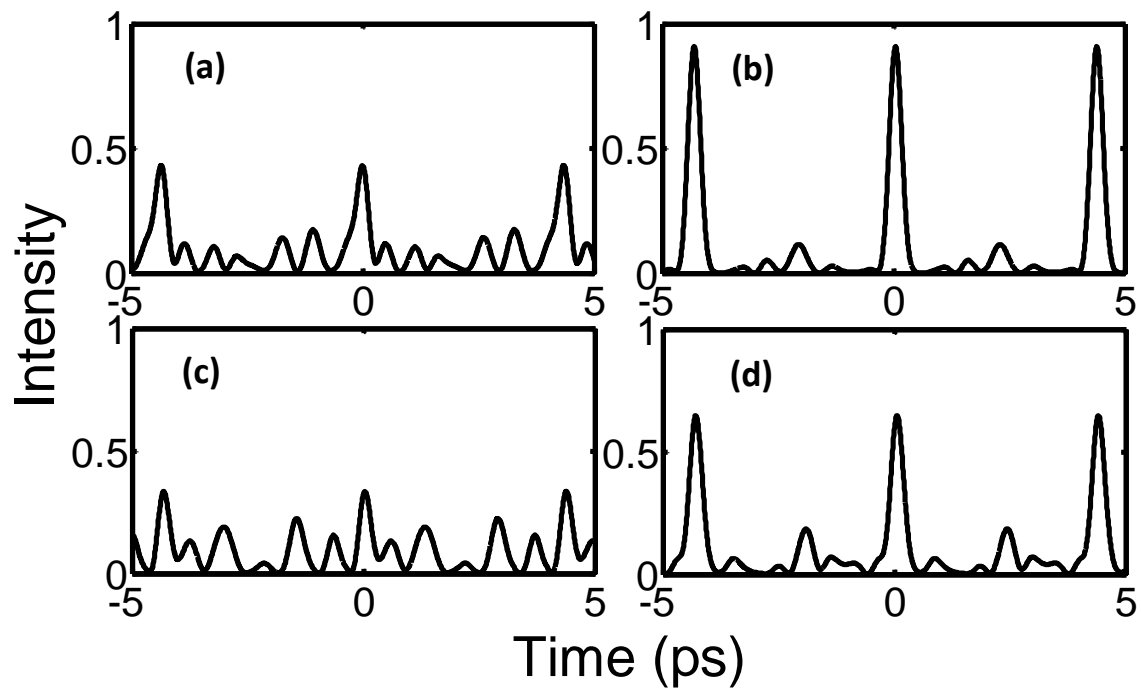


Fig. S2 Selected simulated intensity profiles with uncorrelated random spectral phases that are uniformly distributed in the range of 0 to  $\Delta\varphi = 0.8\pi$ . These plots are normalized to the peak intensity calculated for the case of 0 phase fluctuations.